Simple Strategy to Measure the Contact Resistance between Metals and Doped Organic Films

Anton Kirch,[1] Axel Fischer,[1] Robert Werberger,[1] Shayan Miri Aabi Soflaa,[1] Karolina Maleckaite,[1,2] Paulius Imbrasas,[1] Johannes Benduhn,[1] and Sebastian Reineke[1,*]

[1] *Dresden Integrated Center for Applied Physics and Photonic Materials (IAPP) and Institute of Applied Physics, Technische Universität Dresden, Nöthnitzer Straße 61, Dresden 01187, Germany*

[2] *Center of Physical Sciences and Technology, Sauletekio av. 3, Vilnius LT-10257, Lithuania*

(Received 28 April 2022; accepted 30 June 2022; published 8 September 2022)

Charge injection from electrodes into doped organic films is a widespread technology used in the majority of state-of-the-art organic semiconductor devices. Although such interfaces are commonly considered to form Ohmic contacts via strong band bending, an experiment that directly measures the contact resistance has not yet been demonstrated. In this study, we use a simple metal/doped-organic-semiconductor/metal stack and study its voltage-dependent resistance. A transport-layer thickness variation proves that the experiment presented gains direct access to the contact resistance of the device. We can quantify that for an operating current density of 10 mA/cm^2, the investigated material system exhibits a voltage drop over the metal-organic interface of about 200 mV, which can be reduced by more than one order of magnitude when employing an additional injection layer. The experiment presented proposes a simple strategy to measure the contact resistance between any metal and doped organic film without applying numerical tools or elaborate techniques. Furthermore, the simplistic device architecture allows for very high, homogeneous, and tunable electric fields within the organic layer, which enables a clear investigation of the Poole-Frenkel effect.

DOI: 10.1103/PhysRevApplied.18.034017

I. INTRODUCTION

Doped organic layers enable efficient charge-carrier injection and extraction in various emerging semiconductor devices and have a huge impact on their overall performance. They enable reduced voltage losses at the contact interfaces of photovoltaic (PV) devices [1–4], account for the low operating voltage and reasonable charge balance of light-emitting diodes (LEDs) using organic injection layers [5–7], and enhance the switching speed of organic transistors [8,9]. Thus, a physical understanding and easy measurement routines are crucial to the evolution of this technology.

Any charge injection or extraction between electrodes and organic semiconductors experiences a resistance at the contact interface. Its mechanism is commonly treated in the picture of a metal/semiconductor bilayer rooted in classical semiconductor physics and is standard content in pertinent textbooks [10–12]. Even though amorphous organic semiconductors do not form energy-band structures in the same sense as their crystalline inorganic counterparts, the valence- and conduction-band model is often applied to the distribution of molecular orbitals in amorphous organic films for the sake of simplicity and delivers a readily elaborate physical understanding. In this picture, charge carriers face a potential barrier caused by the difference between the metal work function and the semiconductor energy levels. The tuning of this injection barrier is commonly achieved by energy-level alignment, i.e., by introducing injection layers [13–15], or energy-band bending [11,16–18].

The latter option is mediated via blending the organic semiconductors with dopant molecules [19–21] and provides an enhanced tunneling probability for charge carriers, which is even increased by an image charge potential [22,23]. Depending on the intended majority charge carrier, an electron or hole transport layer requires *n*-type or *p*-type doping, respectively. Organic molecules, such as 7,7,8,8-tetracyano-2,3,5,6-tetrafluoroquinodimethane (F_4-TCNQ) and 2,2'-(perfluoronaphthalene-2,6-diylidene)

*sebastian.reineke@tu-dresden.de

dimalononitrile (F_6-TCNNQ), or halide materials such as $FeCl_3$, are commonly used as *p*-type dopants. Alkali metals such as Li or Cs, on the other hand, are very popular *n*-type dopants [24].

Under standard operating conditions, the interface between metal and doped organic semiconductor is commonly treated as Ohmic and only poses a significant contact resistance below certain bias voltages [25–27]. Naturally, the question arises as to what the term "Ohmic" refers to—indeed, its definition is not intuitive and is sometimes even confused with a connection to Ohm's law. In classical semiconductor physics, the term "Ohmic" describes a contact that poses negligible resistance relative to other resistances in the device regardless of the applied bias polarity and may exhibit nonlinear behavior [10,11]. Is it actually correct that an Ohmic contact can be assumed at common organic LED (OLED) or PV operating conditions? How much voltage drop does the contact resistance cause? The answer is not straightforward and depends on the intended application of the device in question. For high-current applications, such as future electrically driven organic lasers, these voltage losses will be severe [28]. Also, consideration of the resistance contribution of the contacts may aid development of the understanding of OLED operating voltages that deviate from their theoretical limits [29,30], can pave a way toward enhancing transistor performance [31], and can provide further insight into voltage losses in organic or perovskite PV devices [32].

While there have been extensive research efforts to understand metal/doped-organic-semiconductor contacts in detail [32–34], this study presents a direct experimental method to measure the contact resistance of such material combinations. It is a particular challenge to isolate the pure contact behavior, as it is commonly overlaid with the charge-transport characteristics of the investigated device. To overcome this problem, we reduce the device complexity as much as possible: A doped organic semiconductor with variable thickness is sandwiched between two equally thick silver electrodes and its voltage-dependent device characteristics are studied. As a result, the resistance contributions are reduced to the two contacts and a transport layer, the influence of which is controlled via a thickness variation. At the same time, we drastically decrease the active area and use a four-wire crossbar setup to measure high current densities unaffected by parasitic series resistance or self-heating, which would otherwise be detrimental to the experimental outcome. By thoroughly studying the presented model system, we can prove that the manufactured devices follow classical semiconductor physics to a fair extent and that the introduced experimental strategy gains direct access to the contact characteristics of a metal-organic semiconductor interface.

II. METHODS

A. Device fabrication

The hole-only devices are fabricated by thermal evaporation under high vacuum (Kurt J. Lesker Company, evaporation pressure $< 1 \times 10^{-6}$ mbar) on 2.5 cm × 2.5 cm glass substrates (Schott Borofloat33 glass, Prince Optics) of thickness 1.1 mm. The substrates are cleaned in an ultrasonic bath with acetone, ethanol, and deionized water. Aluminum (Chempur) and silver (M&K GmbH Jena), each of thickness 50 nm, are used as bottom and top electrodes. For simplicity, only the silver contacts are shown in Fig. 1. The *p* layer consists of *m*–4,4',4"-Tris(N-3-methylphenyl-N-phenyl-amino)triphenylamine (*m*-MTDATA; Synthon, sublimation cleaned) doped with F_6-TCNNQ (Novaled AG, sublimation cleaned) at a ratio of 4 wt% or Spiro:TTB (Lumtec, sublimation cleaned) doped with $C_{60}F_{36}$ (Ionic Liquids Technologie GmbH, sublimation cleaned), also at 4 wt%. The thickness and deposition rates are monitored using a quartz-crystal microbalance (the full names of the materials and the reverse *J*-*V* characteristics are given in Secs. I and III of the Supplemental Material [35]).

To prohibit air and moisture contamination, the device stacks are encapsulated under a nitrogen atmosphere after fabrication. The encapsulation glass (sodalime glass, AMGTECH Korea) comprises a small cavity above the pixels that prevents direct contact between sensitive materials and the encapsulation glass. It is attached to the substrate using an epoxy resin (XNR5516Z-L and XNR5590, Nagase Europa GmbH).

B. Device evaluation

The devices are placed in a Peltier-element–equipped cryostat that is controlled by a temperature controller (Belektronig, HAT control). The air pressure inside the cryostat is reduced to below 1 mbar using a prevacuum pumping system (Trivac D16B, Germany) to keep a steady temperature and to prevent unwanted air convection. Every measurement is performed using the four-wire method run by a dual-channel source-measure unit (SMU) (Keithley 2602). The impedance measurements are performed using an *LCR* meter (Hewlett Packard 4284A precision *LCR* meter) and a home-built switching matrix to switch between the SMU and the *LCR* meter and to target individual device pixels. The temperature controller, the *LCR* meter, and the SMU are run and controlled by the SweepMe! software tool [36], which enables automated measurement protocols.

C. Equivalent-circuit modeling

The LTspice software (Linear Technology) is used for modeling the equivalent circuit presented in Fig. 1(d) with one fixed set of parameters to achieve all of the model

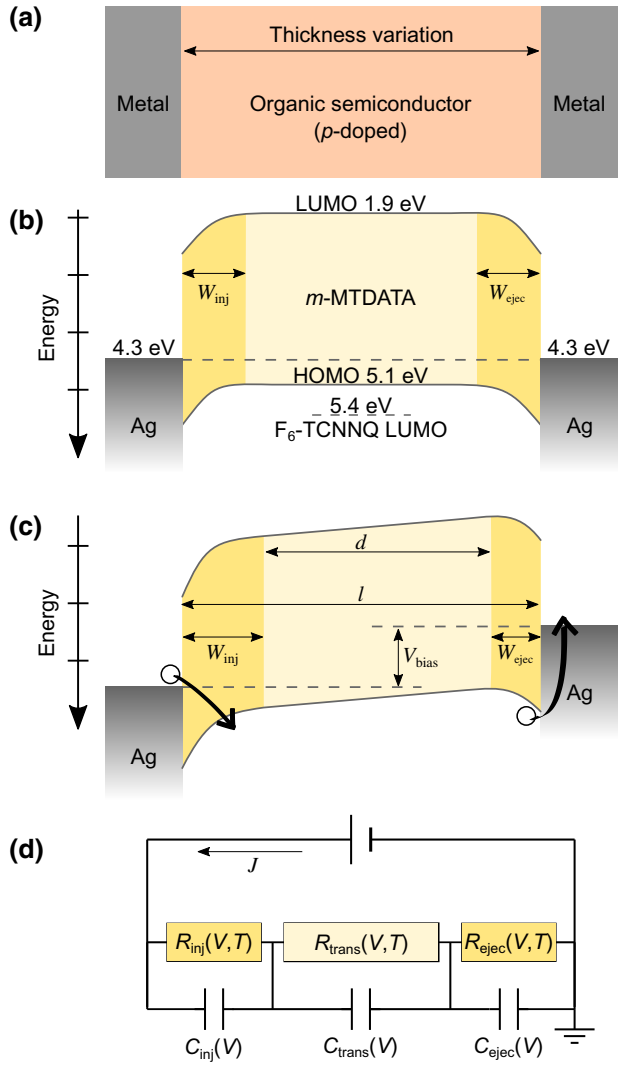

FIG. 1. (a) The device design: a simple metal/doped-organic-semiconductor/metal stack with a variation of the semiconductor thickness. (b) The energy-level diagram at short circuit: The p doping induces band bending and depletion regions at the interfaces. The energy levels are taken from Refs. [41–43]. (c) The energy-level diagram under applied bias. (d) The equivalent-circuit model: the physical characteristics of the presented stack can be described by a simple series of contact and transport equivalent circuits, each represented by a parallel RC element.

results (cf. Table I). In contrast to an analytical PYTHON code, LTspice can self-consistently iterate solutions to model voltage-dependent impedance measurements, as presented in Fig. 4.

III. RESULTS

A. Device architecture

Figures 1(a) and 1(b) present the device architecture with a p-doped organic semiconductor (m-MTDATA:F_6-TCNNQ, 4 wt%) evaporated between two silver electrodes. The doping ratio is chosen high enough to yield a low charge-carrier injection-extraction barrier but also low enough to sustain a medium doping efficiency [20,37]. The semiconductor thickness is varied from 50 nm to 400 nm to study the impact of the charge-transport resistance. This strategy is similar to the concept of a transmission-line method (TLM) experiment often performed with transistors [38–40]. The crucial differences are, first, a drastically reduced device complexity, sporting no dependence on geometry or charge-carrier accumulation. Second, the semiconductor thickness in our experiments is orders of magnitudes below a horizontal organic transistor channel length. The transport resistance becomes, as presented below, almost insignificant for the thin devices used in our experiments. This enables a direct and voltage-dependent contact-resistance measurement without extrapolation to zero semiconductor thickness as performed in a TLM experiment.

TABLE I. The global parameter set used for the equivalent-circuit modeling with LTspice.

Diode ideality factor	n_i	1
Tunneling scaling factor	c	2×10^{-1}
Tunneling-scale conductivity	$\sigma_{0,R}$	4×10^3 mS cm^{-2}
Diode-scale current density	$j_{0,S}$	5×10^2 mA cm^{-2}
Interface potential barrier	V_{BI}	0.35 V
Scale mobility	μ_0	2×10^{-1} cm^{2}V^{-1}s^{-1}
Scale doping concentration	$N_{A,0}$	1×10^{19} cm^{-3}
Relative permittivity	ϵ_r	3.5
Doping activation energy	$E_{A,a}$	25 meV
Mobility activation energy	$E_{\mu,a}$	0.3 eV

The minimal transport layer is chosen to be 50 nm, as films below this thickness become increasingly prone to short-circuit failures. Furthermore, any spatial overlap of the two depletion regions must be avoided to keep the device physics clear. With typical values for our material system such as the relative permittivity of a typical organic semiconductor, $\epsilon_r \approx 3$ [24], the intrinsic potential barrier at the interface $V_{\mathrm{BI}} = 0.5$ eV, and the ionized acceptor concentration $N_A = 1 \times 10^{18}$ cm^{-3}, the depletion width W of one contact can be estimated at $V = 0$ to range around 4 nm:

$$W = \sqrt{\frac{2\epsilon_0\epsilon_r(V_{\mathrm{BI}} - V)}{eN_A}} \approx 4 \text{ nm}. \tag{1}$$

The depletion width W additionally depends on the applied bias, as schematically indicated in Fig. 1(c). Nevertheless, a minimum transport-layer thickness of 50 nm safely rules out depletion-region interference.

The utilization of a single doped organic film guarantees very homogeneous current density and electric field distributions within the device, which are not compromised by additional intrinsic layers or organic-organic interfaces in the film [44,45]. This is proven by current

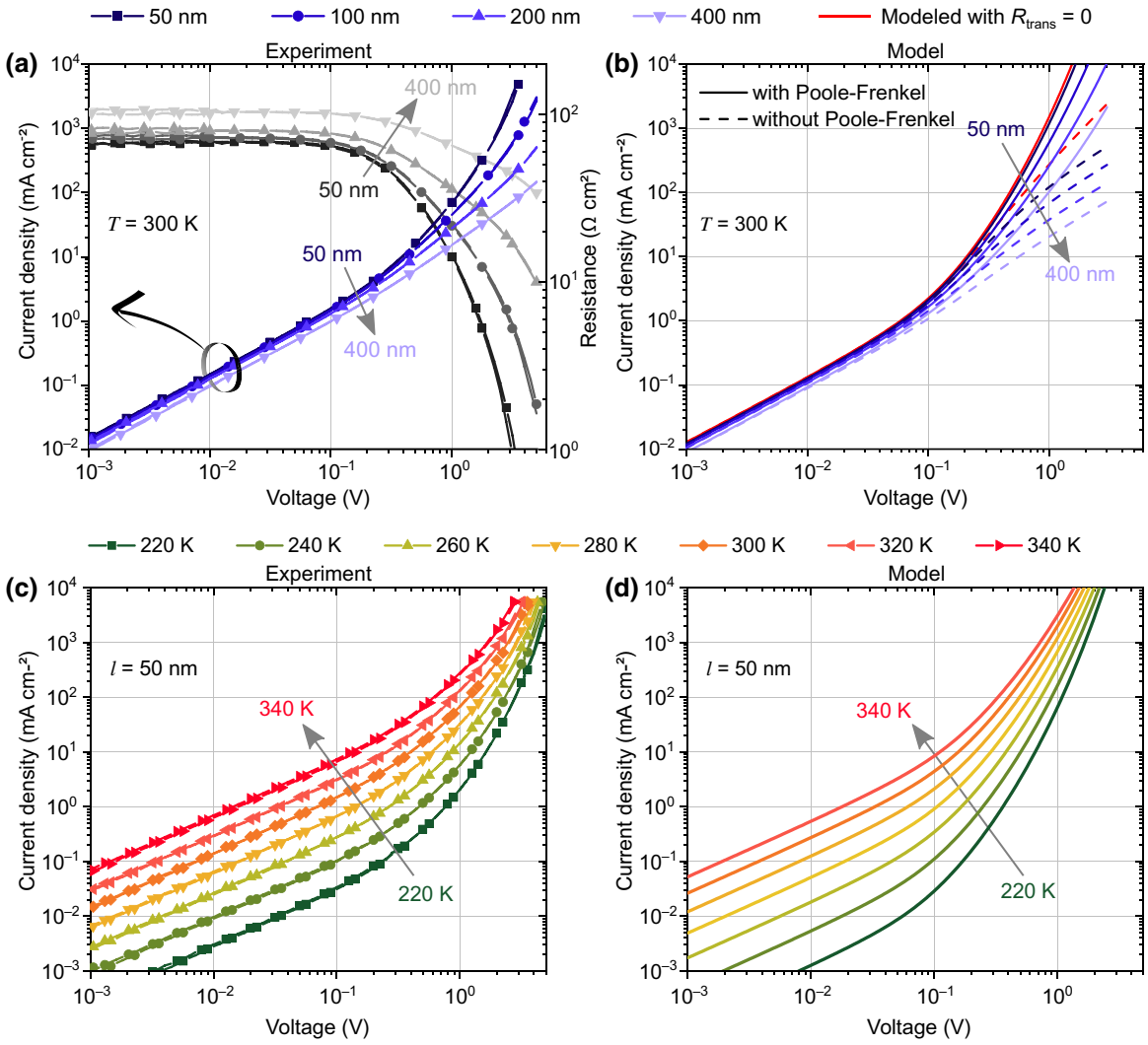

FIG. 2. (a),(b) The dc J-V characteristics scanned back and forth at $T = 300$ K for a thickness variation of the organic semiconductor film: its R-V representation is also represented in (a). (c),(d) The dc J-V characteristics for the $l = 50$ nm device at various temperatures. Experimental results are presented in (a) and (c), while data from the equivalent-circuit modeling are shown in (b) and (d).

density versus voltage (J-V) measurements for different sample areas, which are all found to coincide closely (cf. Sec. IV of the Supplemental Material [35]). For the experiments presented throughout this study, we use the smallest realized cross-section area of 0.09 mm^2 to resolve the lowest possible current densities and to prevent self-heating-induced inhomogeneities scaling with the active area dimension [46].

B. Resistance measurements

A four-wire J-V scan is run back and forth in a Peltier-element–based cryostat under vacuum (below 1 mbar) to ensure stable thermal conditions. Details of the four-wire setup are introduced in Ref. [47]. The technique enables more accurate measurements excluding external series resistances that jeopardize a precise capacitance analysis. This is essential for observing the intended characteristics.

Figure 2(a) presents the measurement results for all four devices at a constant temperature $T = 300$ K. The blue-shaded lines show the J-V characteristics and the grayscale curves show the same data set in resistance representation, $R = V/J$. Only a very slight hysteresis, which is scaling with increasing current density, is detected. It can be identified more clearly in Fig. S2 of the Supplemental Material [35]. Electrothermal feedback, which causes a deviation between the backward and forward J-V measurement directions, can therefore be rendered unimportant for the overall data analysis [47].

For $V < 300$ mV, the J-V curves of the four different transport-layer thicknesses differ only slightly. This indicates that they are governed by the contact resistance between the metal and the doped organic semiconductor

at low voltages. If the transport resistance posed a major contribution, the transport-layer variation by a factor of 8 would cause a respective line separation. This is not the case. While the 400-nm device shows a slight current density and resistance deviation, the three thinnest devices can merely be kept apart.

For $V > 300$ mV, the resistance of all the devices plummets. Also, the lines start to separate drastically according to their transport-layer thickness, i.e., the contact resistance drops below the transport resistance, which starts to govern the device characteristics.

Figure 1(d) presents an equivalent circuit that can be used to better understand this behavior. Any of the three introduced device layers, i.e., the *injection*, *transport*, and *ejection* layers, needs to include a resistive component. The circuit model also emphasizes that our devices sport two contact resistances, one at each metal/organic film interface. The experiment, therefore, measures the sum of a forward and reverse contact-resistance contribution.

The ejection and injection interfaces each need to be represented by a variable resistor, R_{inj} and R_{ejec}, as all devices are limited by their contact resistance at low bias voltages. Instead of an accurate but complex interface analysis, only the governing physical concepts are included. This is sufficient to understand the device physics, as we see that our model successfully represents all experimental trends. Accurate quantitative tracing of the experimental results is not our intention here. The charge-carrier injection and ejection currents can be understood as Schottky contacts [48] and are described by a tunneling term [49] and an ideal diode equation [10], which is reduced by the effective, i.e., image-force-reduced, potential barrier at the interface V_{BI}:

$$j_{\mathrm{Diode}} = j_{0,S} \exp\left(\frac{-eV_{\mathrm{BI}}}{n_i k_B T}\right)\left[\exp\left(\frac{eV}{n_i k_B T}\right) - 1\right], \tag{2}$$

$$j_{\mathrm{Tun}} = \sigma_{0,R} V \exp\left(\frac{-eV_{\mathrm{BI}}}{n_i k_B T}\right)\left[\exp\left(c\frac{\sqrt{|V|}}{k_B T}\right) - 1\right]. \tag{3}$$

The parameter k_B depicts the Boltzmann constant, T is the device temperature, n_i is the diode ideality factor, e is the elementary charge, c is an arbitrary tunneling scaling factor, V is the voltage drop across the respective resistor element, $j_{0,S}$ is the scale current density, and $\sigma_{0,R}$ is the scale conductivity. Note that $\sigma_{0,R}V$ again yields a current density, which is the current density of the tunneling term. The global model parameters are given in Table I.

The symmetric architecture yields a symmetric device behavior, as shown in Fig. S2 of the Supplemental Material [35]. Therefore, both contacts need to be described by the same formula. We choose a simple superposition, which only differs in the respective signs for injection- and ejection-current densities:

$$j_{\mathrm{inj}} = j_{\mathrm{Tun}}(V_{\mathrm{inj}}) - j_{\mathrm{Diode}}(-V_{\mathrm{inj}}), \tag{4}$$

$$j_{\mathrm{ejec}} = -j_{\mathrm{Tun}}(-V_{\mathrm{ejec}}) + j_{\mathrm{Diode}}(V_{\mathrm{ejec}}). \tag{5}$$

Both contact elements are susceptible to the voltage drop across the respective interface and decrease exponentially, as found by the experimental data. An increasing bias causes a more pronounced band bending at the injection interface, which increases the tunneling probability. Also, the Schottky barrier at the ejection interface is reduced [50]. Both processes make the total contact resistance drop with increasing bias voltage.

The transport resistance must also be represented by a variable-resistor element R_{trans}, since the devices depend on the thickness of the organic film at elevated bias voltages. Due to the high doping concentration throughout the entire organic semiconductor film, space-charge-limited effects cannot play a pivotal part and the transport resistance is assumed to be purely Ohmic (for the detailed reasoning, see Sec. II of the Supplemental Material [35]). The current density passing R_{trans} reads

$$j_{\mathrm{trans}} = e\, N_A \mu \frac{V_{\mathrm{trans}}}{d}, \tag{6}$$

where $d = l - W_{\mathrm{inj}} - W_{\mathrm{ejec}}$ is the thickness of the nondepleted transport layer, in which l is the total thickness of the doped organic film [cf. Fig. 1(c)], V_{trans} is the voltage drop across the transport layer, and N_A is the temperature-activated ionized dopant concentration, equal to the effective charge-carrier density (cf. Sec. I of the Supplemental Material [35] and the parameters in Table I):

$$N_A = N_{A,0} \exp\left(\frac{-E_{A,a}}{k_B T}\right). \tag{7}$$

As temperature- and field-dependent experiments are carried out and they alter the device characteristics, the mobility term $\mu = \mu(T, V)$ must contain a temperature and an electric field dependency to successfully model the experimental results. $R_{\mathrm{transport}}$ has to drop with increasing bias, since the J-V curves bend upward when separated according to their transport-layer thickness. This cannot be explained by linear resistance characteristics. The encountered field strength, here exceeding 100 kV/cm, has previously been identified as relevant when studying field-enhanced mobility [51]. The presented device architecture, employing doped films, easily exceeds this value and hints that a large range of sandwich-type devices should be eligible for the simple determination of their contact resistance.

The nonlinear behavior at high electric fields requires a field-induced mobility enhancement, commonly known as

the Poole-Frenkel (PF) effect [11,49]:

$$\mu = \mu_0 \exp\left(\frac{-E_{\mu,a}}{k_B T}\right) \exp\left(\beta\sqrt{\frac{|V_{\text{trans}}|}{d}}\right), \tag{8}$$

$$\beta = \frac{e}{k_B T}\sqrt{\frac{e}{\pi \epsilon_r \epsilon_0}}, \tag{9}$$

where the parameter β is defined in Ref. [52], k_B is the Boltzmann constant, T is the device temperature, ϵ_r is the relative permittivity of the organic film, and $E_{\mu,a}$ is the mobility activation energy. For both dependencies, temperature and electric field, we use simplistic approaches. We are well aware that both dependencies have to be modeled with more complexity if a good agreement between experimental and model results is to be expected. Our model fails at high electric fields, as can be seen by the increasing deviations between Figs. 2(a) and 2(b). This accounts for an oversimplification of the PF term in the equivalent circuit. From the simulated results in Fig. 2(b), comprising both a scenario with and without a PF term, one can estimate the true PF contribution to be in between the two realized modeling scenarios, i.e., a reduction of β would yield better agreement. However, it is not the intention of our investigation to pursue this. Nevertheless, it is worth pointing out that our presented experimental approach allows the study of the PF effect in organic semiconductors with very high precision, as demonstrated, e.g., by Blom and coworkers [51,53]. While stacked films in complete semiconductor devices induce a varying electric field in the vertical direction, the geometry realized here ensures a very homogeneous field strength throughout the transport layer.

The thinner the transport layer, the smaller is its resistance contribution. A thinner device follows the pure contact-resistance characteristics up to higher current densities than a thick device. Hence the isolated contact resistance can be estimated best from the $l = 50$ nm sample. Figure 2(b) presents the model scenario with vanishing transport influence, $R_{\text{trans}} = 0$, indicated in red. It is, therefore, safe to deduce that the contact-resistance characteristics must be nonlinear and must stay reasonably close to the $l = 50$ nm device up to about 100 mA/cm^2. This range is sufficient to quantify the contact resistance for most organic electronics applications.

Both the contact-resistance and the transport characteristics are susceptible to temperature, as shown in Figs. 2(c) and 2(d). That is, the mobility in Eq. (8) is enhanced by an Arrhenius term, as are the tunneling and diode characteristics in Eqs. (2) and (3). The experimental trend of temperature-induced conductivity is replicated successfully by the model.

The simulation of the three resistance contributions displayed in Fig. 1(d) is evaluated with LTspice and allows us to quantify each of them separately. Figure S9 in the Supplemental Material [35] presents the modeled contributions and makes it plain that the injection and ejection resistances govern the device behavior at low voltages. For $V > 100$ mV, all three resistances start to drop dramatically. The two contact-resistance contributions, R_{inj} and R_{ejec}, however, drop faster than the transport resistance, which takes over the device characteristics at increasing bias. Figure S9 in the Supplemental Material [35] also implies that injection and ejection follow roughly the same trend at low voltages, owing to their mutual exponential nature. Thus, an estimation to identify either the injection (important for OLEDs) or ejection resistance (important for PV) from the measurements would be $R_{\text{inj}} \approx R_{\text{ejec}}$ at low voltages.

C. Impedance measurements

The resistivity measurements presented above are based on the assumption that we are indeed probing the pure contact resistance. To gather further evidence on that assertion, impedance measurements are performed in this section. We demonstrate that we can disclose the contact and geometrical capacitance and that the investigated devices show two depletion regions, two voltage-dependent capacitance plateaus, and a temperature- and thickness-dependent behavior, all of which follow basic semiconductor physics.

Figures 3(a) and 3(c) present the experimental capacitance density versus frequency (C-f) characteristics at zero bias voltage $V = 0$ with varying thickness and temperature, respectively. Details of the capacitance-density evaluation from a four-wire measurement are given in Sec. V of the Supplemental Material [35]. Again, it is very important to employ a four-wire measuring technique to keep parasitic series resistance out of the evaluation.

The experimental results present two distinct capacitance-density plateaus. This behavior can be understood if treating any of the three distinct layers within the device not only as having a resistive representation but as an RC element [cf. Fig. 1(d)]. At $V = 0$, the depletion regions of injection and ejection have the same width W and, treated like plate capacitors in the equivalent circuit, also the same capacitance density $C_{\text{inj}} = C_{\text{ejec}}$:

$$C_{\text{inj}} = \frac{\epsilon_0 \epsilon_r}{W_{\text{inj}}}, \tag{10}$$

$$C_{\text{ejec}} = \frac{\epsilon_0 \epsilon_r}{W_{\text{ejec}}}. \tag{11}$$

At low frequencies, the reactance of the transport capacitance C_{trans} is high and the charge-carrier flow is, rather, mediated via R_{trans}. As a result, the device capacitance is governed by the injection and ejection capacitances. At room temperature, with no bias voltage, negligible transport resistance, and low frequencies, the device

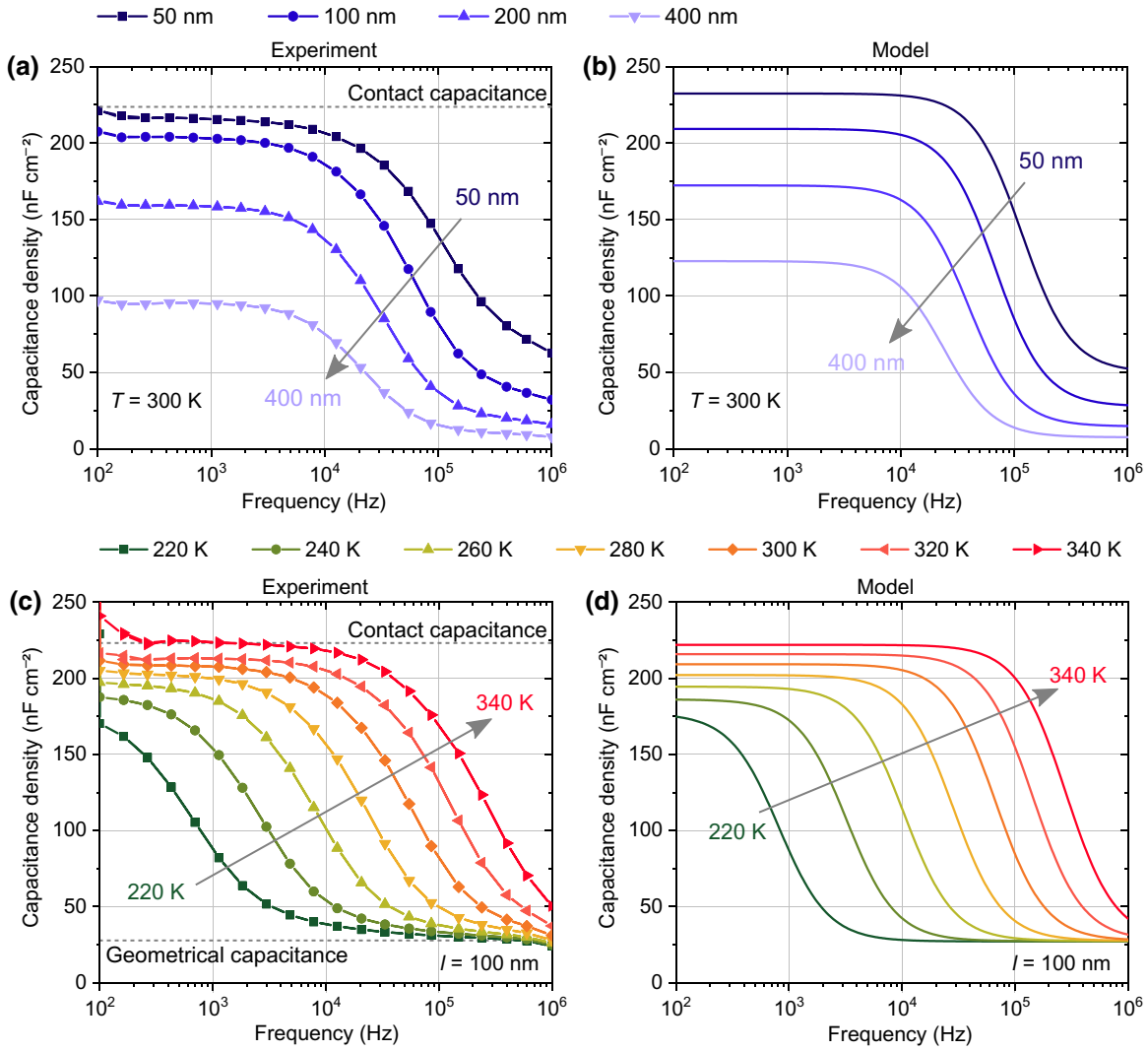

FIG. 3. The impedance characteristics at $V = 0$. (a),(b) Data at $T = 300$ K for a thickness variation of the organic semiconductor. (c),(d) Data for the $l = 100$ nm device at various temperatures. Experimental results are presented in (a) and (c), while data from the equivalent-circuit modeling are shown in (b) and (d).

capacitance density can be estimated as

$$C(f \ll 1\ \text{kHz}) \approx \left(\frac{1}{C_{\text{inj}}} + \frac{1}{C_{\text{ejec}}}\right)^{-1} \overset{V=0}{=} \frac{C_{\text{contact}}}{2}, \tag{12}$$

where $C_{\text{inj}} = C_{\text{ejec}} = C_{\text{contact}}$ due to the device symmetry at $V = 0$. From Fig. 3(a), however, it is apparent that Eq. (12) holds merely for low transport resistances, i.e., very thin transport layers. The thicker the transport layer, the higher is its resistance. As a result, even at low frequencies, the transport capacitance mediates a significant share of the device current and reduces the total capacitance density. Thus, the capacitance at low frequencies is decreasing with an increasing transport-layer thickness and the pure contact capacitance can only be measured for transport layers tending toward zero thickness, i.e., the $l = 50$ nm device.

At high frequencies, the transport capacitance becomes dominant, as its reactance drops below the resistance of the transport layer. Since the depletion region is smaller than the transport-layer thickness d of all of the devices [cf. Eq. (1)], the contact capacitance is expected to be higher than the transport capacitance. As a result, the total capacitance density falls to a second plateau at high frequencies. This plateau is governed by the device geometry (organic film thickness) and is called the *geometrical capacitance density* C_{geo}:

$$C(f \gg 1\ \text{kHz}) = C_{\text{geo}} = \left(\frac{1}{C_{\text{inj}}} + \frac{1}{C_{\text{trans}}} + \frac{1}{C_{\text{ejec}}}\right)^{-1}. \tag{13}$$

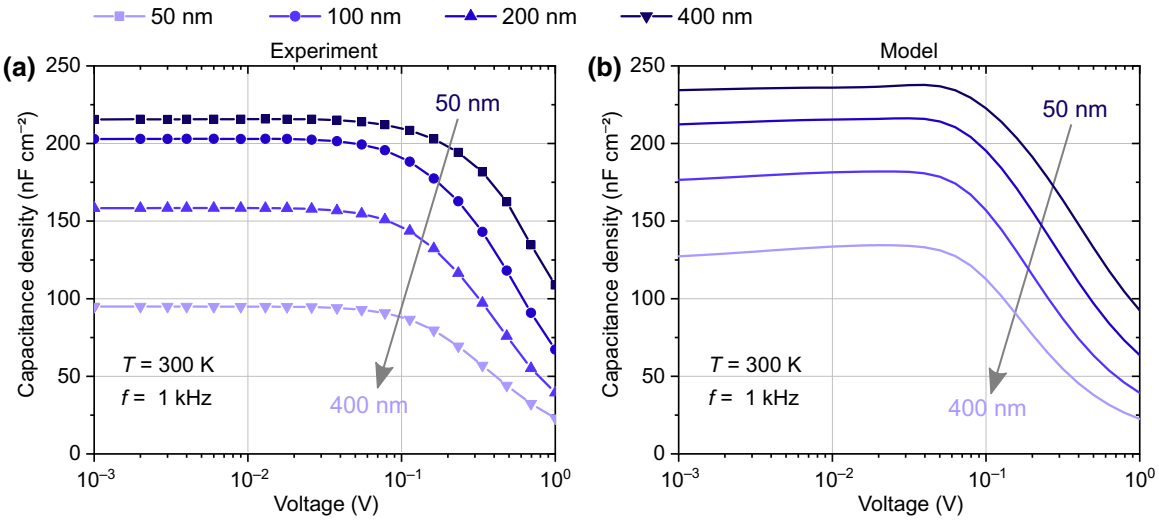

FIG. 4. The impedance characteristics at $T = 300$ K and $f = 1$ k Hz for a thickness variation of the transport channel: (a) experimental data; (b) results from the equivalent circuit presented in Fig. 1(d).

The transport capacitance density C_{trans} is a function of the transport-layer thickness d and is, as a simplistic approach, also represented by a plate capacitor in the equivalent circuit given in Fig. 1(d):

$$C_{\text{trans}} = \frac{\epsilon_0 \epsilon_r}{d}. \tag{14}$$

To support the understanding presented above, impedance spectroscopy is also carried out with a fixed organic film thickness ($l = 100$ nm) for different temperatures. Figure 3(c) presents the transition interval between the contact and the geometrical capacitance-density plateau as being temperature dependent. This can be mainly understood by considering $R_{\text{trans}} = R_{\text{trans}}(V, T)$ as a function of temperature according to Eqs. (6) and (8). At low temperatures, R_{trans} is high and the current is mediated earlier via the transport capacitance, the reactance of which does not scale directly with temperature. For increasing temperatures, R_{trans} decreases and the cutoff frequency f_G for the transport RC element increases:

$$f_{G,\text{trans}}(V, T) = \frac{1}{2\pi R_{\text{trans}}(V, T) C_{\text{trans}}(V)}. \tag{15}$$

Figures 3(b) and 3(d) present the results from the equivalent-circuit model performed with LTspice. The qualitative trends of the experiments are reproduced and even quantitatively the results are similar. The transition characteristics in the experiment, however, are sloping more gently than in the model. The equivalent circuit follows the Schottky assumption of three distinct layers having an abrupt change from depleted- to neutral-semiconductor characteristics. This is a simplification that allows the modeling of the two different frequency-dependent operating regimes. In the real device, however, the transition between the depleted and neutral regions is smooth and hence the impedance characteristics are smeared out with respect to the model.

D. Depletion-zone variation

The impedance spectroscopy experiments discussed above are performed at zero bias voltage, $V = 0$. Here, the contact capacitances at either side of the device must be equal, according to the symmetry of the device. The depletion width W, however, depends on the voltage drop over the respective layer [cf. Eq. (1) and Fig. 1(c)]. The idea of the subsequent measurement is to investigate the influence of voltage on the contact capacitances.

To access the isolated contact capacitance characteristics as well as possible, the experiment is performed at $f = 1$ kHz and room temperature, as deduced from the Sec. III C. Figure 4(a) presents the capacitance density of all four devices versus the applied bias voltage. Using the global set of model parameters displayed in Table I, a short-circuit depletion width (at $V = 0$) of about $W \approx 4$ nm at each interface can be expected. According to Eq. (1) and as indicated in Fig. 1(c), W_{inj} increases and W_{ejec} decreases under forward bias. When considering the contact-limited capacitance at 1 kHz, where the transport capacitance density C_{trans} is assumed to play no pivotal role, the capacitance-density trend can be understood to follow a voltage-dependent version of Eq. (12), i.e.,

$$C(f = 1\ \text{kHz}, V) = \left(\frac{\epsilon_r \epsilon_0}{W_{\text{inj}}(V_{\text{inj}}) + W_{\text{ejec}}(V_{\text{ejec}})} \right), \tag{16}$$

where both W_{inj} and W_{ejec} follow Eq. (1). For low applied bias, the two voltage dependencies apparently cancel each other, as around $V = 0$ their behavior can be approximated

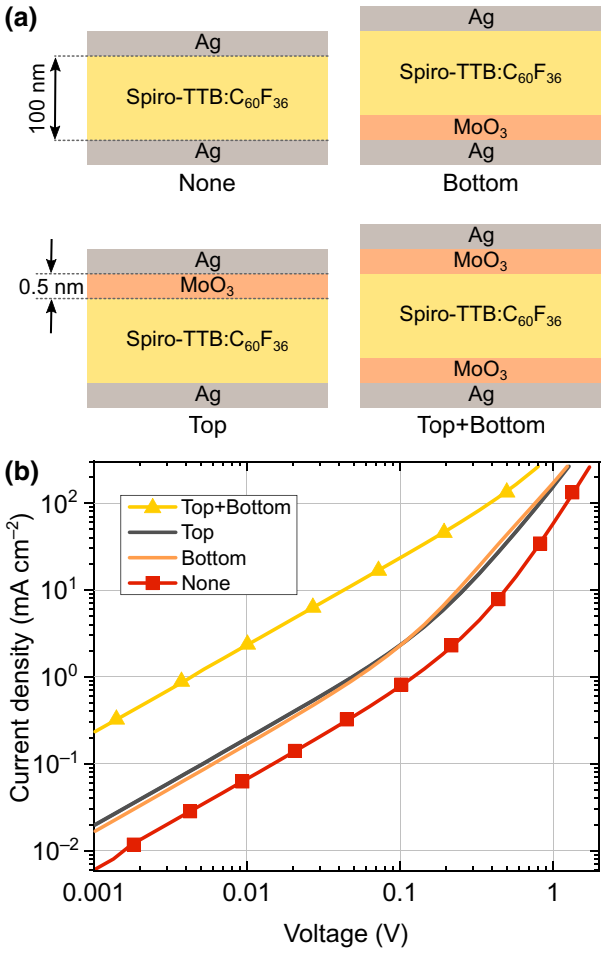

FIG. 5. (a) The investigated stack designs comprising 100 nm of p-doped organic semiconductor and either no or one or two contact enhancement layers of MoO_3 (0.5 nm). (b) The respective J-V characteristics at $T = 300$ K and an illustration of the effect on the measured contact resistance.

as being linear. Beyond an applied bias of about 100 mV, the linear approximation fails and the denominator of Eq. (16) starts to grow. The total capacitance density of the devices drops. The same overall trend can be reproduced by the equivalent-circuit simulation, presented in Fig. 4(b).

E. Demonstration scenario for injection-enhancement quantification

Throughout the preceding sections, an experimental setting is introduced that evidently provides direct access to the contact resistance of a given interface between a metal and a doped organic film. As an outline toward potential application scenarios, in this section we present a short study on the effect of additional interface layers that reduce the contact resistance.

The subsequent experiment uses an equivalently simple stack of 100 nm of Spiro-TTB-doped with $C_{60}F_{36}$ (4 wt%) sandwiched between two silver electrodes. Again, we perform a thickness-dependent J-V analysis and find, as for the m-MTDATA:F_6-TCNNQ devices, that the resistance behavior for $J < 10$ mA/cm^2 is not influenced by the organic layer thickness up to $l = 200$ nm (cf. Sec. VI of the Supplemental Material [35]). That is, direct access to the contact resistance of the device is guaranteed. Now, either at the top, the bottom, or at both contact interfaces, a thin layer (0.5 nm) of molybdenum oxide (MoO_3) is added [cf. Fig. 5(a)], which is commonly used to reduce the contact resistance of p-doped organic semiconductor devices [4,15,54–56]. The data in Fig. 5(b) prove that adding one injection interlayer clearly reduces the contact resistance of the respective interface. There appears to be no significant difference between employing the enhancement layer in the top or bottom configuration. Most likely, the nonenhanced contact governs the contact-resistance characteristics here. The use of MoO_3 on both interfaces reduces the contact resistance at 10 mA/cm^2 by more than one order of magnitude, from about 30 Ω cm^2 to below 3 Ω cm^2. A detailed investigation of this material combination can be found in Sec. VI of the Supplemental Material [35]). In such a fashion, contact-resistance-enhancing strategies can easily be evaluated.

IV. CONCLUSIONS

This paper presents a strategy to measure the isolated contact resistance between metals and doped organic semiconductors up to reasonable device operating conditions. For the investigated model structure of a p-doped film (m-MTDATA:F_6-TCNNQ, 4 wt%) between two silver electrodes, the two metal-organic interfaces cause a potential drop of about 400 mV at 10 mA/cm^2. At this current density, one contact poses therefore a resistance of $R_{\text{contact}} \approx 20$ Ω cm^2. The presented concept requires neither complex experiments nor sophisticated theoretical treatment but is based entirely on an easy-to-perform J-V scan. As a proof of concept, we perform a thorough evaluation for the mentioned hole-only device configuration. We employ resistance and impedance measurements while scanning a variety of device temperatures and organic film thicknesses and successfully compare the results to a simple equivalent circuit realized in LTspice. The model uses one global set of parameters that replicate all the experimental findings. This proves that the measured device characteristics directly disclose the contact behavior of the device up to about 100 mA/cm^2 for the given system, which is sufficient for most operating scenarios in LEDs or solar cells. We further present how our measurement concept can help other groups evaluate their contact enhancement strategies by investigating the influence of molybdenum oxide as an injection layer in a second material system comprising Spiro-TTB doped with $C_{60}F_{36}$ and silver electrodes. The presented device architecture turns out to achieve extremely strong and homogeneous electric fields, which

allows us to specifically study the Poole-Frenkel effect in organic semiconductors.

All materials, code, and data are available on reasonable request.

ACKNOWLEDGMENTS

This work was supported by the German Research Foundation (DFG) within the project HEFOS (Grant No. FI 2449/1-1) and by EFOD (Grant No. RE 3198/6-1). We thank Andreas Wendel and Tobias Günther for manufacturing the devices.

A.F. conceptualized the study. A.K. and A.F. analyzed the data and performed the LTspice implementation. A.K. prepared the graphs and mainly wrote the manuscript. A.F., R.W., P.I., and K.M. set up and conducted the experiments. J.B. and S.M. contributed major ideas to the physical understanding. S.R. supervised the project. All authors discussed the results, reviewed the manuscript, and contributed to the text.

Dr. Axel Fischer is cofounder of "SweepMe! GmbH," which provided the measurement software "SweepMe!" [36]. The name of the program is given in the text. The other authors declare no conflicts of interest.

[1] Y. Guo, W. Sato, K. Shoyama, and E. Nakamura, Sulfamic acid-catalyzed lead perovskite formation for solar cell fabrication on glass or plastic substrates, J. Am. Chem. Soc. **138**, 5410 (2016).

[2] V. A. Trukhanov, V. V. Bruevich, and D. Y. Paraschuk, Effect of doping on performance of organic solar cells, Phys. Rev. B **84**, 205318 (2011).

[3] J.-W. Xiao, C. Shi, C. Zhou, D. Zhang, Y. Li, and Q. Chen, Contact engineering: Electrode materials for highly efficient and stable perovskite solar cells, Solar RRL **1**, 1700082 (2017).

[4] K. Ding and S. R. Forrest, Reducing Energy Losses at the Organic–Anode-Buffer Interface of Organic Photovoltaics, Phys. Rev. Appl. **13**, 054046 (2020).

[5] M. Yahya and M. R. Fadavieslam, The effects of argon plasma treatment on ITO properties and the performance of OLED devices, Opt. Mater. (Amst.) **120**, 111400 (2021).

[6] M. T. Khan, M. Salado, A. Almohammedi, S. Kazim, and S. Ahmad, Elucidating the impact of charge selective contact in halide perovskite through impedance spectroscopy, Adv. Mater. Interfaces **6**, 1901193 (2019).

[7] H. Wei, R. Zhang, G. Huang, C. Lv, and J. Tang, Highly stable and efficient tandem white light emitting diodes based on efficient electron injection and transport, J. Mater. Chem. C **10**, 5994 (2022).

[8] M. Waldrip, O. D. Jurchescu, D. J. Gundlach, and E. G. Bittle, Contact resistance in organic field-effect transistors: Conquering the barrier, Adv. Funct. Mater. **30**, 1904576 (2020).

[9] F. Dollinger, K.-G. Lim, Y. Li, E. Guo, P. Formánek, R. Hübner, A. Fischer, H. Kleemann, and K. Leo, Vertical organic thin-film transistors with an anodized permeable base for very low leakage current, Adv. Mater. **31**, 1900917 (2019).

[10] S. M. Sze, Y. Li, and K. K. Ng, *Physics of Semiconductor Devices* (John Wiley & Sons, Hoboken, New Jersey, 2021).

[11] A. Köhler and H. Bässler, *Electronic Processes in Organic Semiconductors: An Introduction* (Wiley-VCH, Weinheim, Germany, 2015).

[12] S. R. Forrest, *Organic Electronics: Foundations to Applications* (OUP Oxford, Oxford, United Kingdom, 2020).

[13] A. Kumatani, Y. Li, P. Darmawan, T. Minari, and K. Tsukagoshi, On practical charge injection at the metal/organic semiconductor interface, Sci. Rep. **3**, 1026 (2013).

[14] D. Kumaki, T. Umeda, and S. Tokito, Reducing the contact resistance of bottom-contact pentacene thin-film transistors by employing a MoO_x carrier injection layer, Appl. Phys. Lett. **92**, 013301 (2008).

[15] N. B. Kotadiya, H. Lu, A. Mondal, Y. Ie, D. Andrienko, P. W. M. Blom, and G.-J. A. H. Wetzelaer, Universal strategy for Ohmic hole injection into organic semiconductors with high ionization energies, Nat. Mater. **17**, 329 (2018).

[16] J. Blochwitz, T. Fritz, M. Pfeiffer, K. Leo, D. M. Alloway, P. A. Lee, and N. R. Armstrong, Interface electronic structure of organic semiconductors with controlled doping levels, Org. Electron. **2**, 97 (2001).

[17] A. Kahn, N. Koch, and W. Gao, Electronic structure and electrical properties of interfaces between metals and π-conjugated molecular films, J. Polym. Sci. Part B: Polym. Phys. **41**, 2529 (2003).

[18] E. Auroux, A. Sandström, C. Larsen, E. Zäll, P. Lundberg, T. Wågberg, and L. Edman, Evidence and effects of ion transfer at active-material/electrode interfaces in solution-fabricated light-emitting electrochemical cells, Adv. Electron. Mater. **7**, 2100253 (2021).

[19] K. Walzer, B. Maennig, M. Pfeiffer, and K. Leo, Highly efficient organic devices based on electrically doped transport layers, Chem. Rev. **107**, 1233 (2007).

[20] M. L. Tietze, L. Burtone, M. Riede, B. Lüssem, and K. Leo, Fermi level shift and doping efficiency in p-doped small molecule organic semiconductors: A photoelectron spectroscopy and theoretical study, Phys. Rev. B **86**, 035320 (2012).

[21] M. L. Tietze, J. Benduhn, P. Pahner, B. Nell, M. Schwarze, H. Kleemann, M. Krammer, K. Zojer, K. Vandewal, and K. Leo, Elementary steps in electrical doping of organic semiconductors, Nat. Commun. **9**, 1182 (2018).

[22] B. N. Limketkai and M. A. Baldo, Charge injection into cathode-doped amorphous organic semiconductors, Phys. Rev. B **71**, 085207 (2005).

[23] A. R. Hosseini, M. H. Wong, Y. Shen, and G. G. Malliaras, Charge injection in doped organic semiconductors, J. Appl. Phys. **97**, 023705 (2005).

[24] W. Brütting, C. Adachi, and R. J. Holmes, *Physics of Organic Semiconductors* (Wiley-VCH, Weinheim, Germany, 2012), 2nd ed.

[25] G. Liaptsis and K. Meerholz, Crosslinkable TAPC-based hole-transport materials for solution-processed organic light-emitting diodes with reduced efficiency roll-off, Adv. Funct. Mater. **23**, 359 (2013).

[26] S. Züfle, S. Altazin, A. Hofmann, L. Jäger, M. T. Neukom, W. Brütting, and B. Ruhstaller, Determination of charge

transport activation energy and injection barrier in organic semiconductor devices, J. Appl. Phys. **122**, 115502 (2017).
[27] H. Siemund and H. Göbel, Numerical Simulation of organic light-emitting diodes with insulating cathode buffer layer, IEEE Trans. Electron Devices **63**, 3700 (2016).
[28] S. Meister, R. Brückner, M. Sudzius, H. Fröb, and K. Leo, Optically pumped lasing of an electrically active hybrid OLED-microcavity, Appl. Phys. Lett. **112**, 113301 (2018).
[29] R. Meerheim, K. Walzer, G. He, M. Pfeiffer, and K. Leo, in *Photonics Europe*, edited by P. L. Heremans, M. Muccini, and E. A. Meulenkamp (Strasbourg, France, 2006), p. 61920P.
[30] R. Meerheim, S. Scholz, S. Olthof, G. Schwartz, S. Reineke, K. Walzer, and K. Leo, Influence of charge balance and exciton distribution on efficiency and lifetime of phosphorescent organic light-emitting devices, J. Appl. Phys. **104**, 014510 (2008).
[31] J. W. Borchert, R. T. Weitz, S. Ludwigs, and H. Klauk, A critical outlook for the pursuit of lower contact resistance in organic transistors, Adv. Mater. **34**, 2104075 (2022).
[32] O. J. Sandberg, A. Sundqvist, M. Nyman, and R. Österbacka, Relating Charge Transport, Contact Properties, and Recombination to Open-Circuit Voltage in Sandwich-Type Thin-Film Solar Cells, Phys. Rev. Appl. **5**, 044005 (2016).
[33] S. Altazin, R. Clerc, R. Gwoziecki, D. Boudinet, G. Ghibaudo, G. Pananakakis, I. Chartier, and R. Coppard, Analytical modeling of the contact resistance in top gate/bottom contacts organic thin film transistors, Org. Electron. **12**, 897 (2011).
[34] M. Oehzelt, N. Koch, and G. Heimel, Organic semiconductor density of states controls the energy level alignment at electrode interfaces, Nat. Commun. **5**, 4174 (2014).
[35] See the Supplemental Material at http://link.aps.org/supplemental/10.1103/PhysRevApplied.18.034017 for further experimental results, details on data evaluation and materials.
[36] A. Fischer and F. Kaschura, SweepMe! A multi-tool measurement software, www.sweep-me.net (2020).
[37] S. Olthof, W. Tress, R. Meerheim, B. Lüssem, and K. Leo, Photoelectron spectroscopy study of systematically varied doping concentrations in an organic semiconductor layer using a molecular p-dopant, J. Appl. Phys. **106**, 103711 (2009).
[38] G. Reeves and H. Harrison, Obtaining the specific contact resistance from transmission line model measurements, IEEE Electron Device Lett. **3**, 111 (1982).
[39] S.-W. Rhee and D.-J. Yun, Metal-semiconductor contact in organic thin film transistors, J. Mater. Chem. **18**, 5437 (2008).
[40] G. Horowitz, Interface modification for tuning the contact resistance of metal/organic semiconductor junctions, Open Appl. Phys. J. **4**, 2 (2011).
[41] M. Aonuma, T. Oyamada, H. Sasabe, T. Miki, and C. Adachi, Material design of hole transport materials capable of thick-film formation in organic light emitting diodes, Appl. Phys. Lett. **90**, 183503 (2007).
[42] H. B. Michaelson, The work function of the elements and its periodicity, J. Appl. Phys. **48**, 4729 (1977).
[43] P. K. Koech, A. B. Padmaperuma, L. Wang, J. S. Swensen, E. Polikarpov, J. T. Darsell, J. E. Rainbolt, and D. J. Gaspar, Synthesis and application of 1, 3, 4, 5, 7, 8-hexafluorotetracyanonaphthoquinodimethane (F6-TNAP): A conductivity dopant for organic light-emitting devices, Chem. Mater. **22**, 3926 (2010).
[44] Y. Zheng, A. Fischer, N. Sergeeva, S. Reineke, and S. C. B. Mannsfeld, Exploiting lateral current flow due to doped layers in semiconductor devices having crossbar electrodes, Org. Electron. **65**, 82 (2019).
[45] A. Fischer, P. Pahner, B. Lüssem, K. Leo, R. Scholz, T. Koprucki, J. Fuhrmann, K. Gärtner, and A. Glitzky, Self-heating effects in organic semiconductor crossbar structures with small active area, Org. Electron. **13**, 2461 (2012).
[46] A. Kirch, A. Fischer, M. Liero, J. Fuhrmann, A. Glitzky, and S. Reineke, Electrothermal tristability causes sudden burn-in phenomena in organic LEDs, Adv. Funct. Mater. **31**, 2106716 (2021).
[47] A. Kirch, A. Fischer, M. Liero, J. Fuhrmann, A. Glitzky, and S. Reineke, Experimental proof of Joule heating-induced switched-back regions in OLEDs, Light: Sci. Appl. **9**, 1 (2020).
[48] Y. Xu, H. Sun, and Y.-Y. Noh, Schottky barrier in organic transistors, IEEE Trans. Electron Devices **64**, 1932 (2017).
[49] Z. B. Wang, M. G. Helander, M. T. Greiner, J. Qiu, and Z. H. Lu, Carrier mobility of organic semiconductors based on current-voltage characteristics, J. Appl. Phys. **107**, 034506 (2010).
[50] P. Pahner, H. Kleemann, L. Burtone, M. L. Tietze, J. Fischer, K. Leo, and B. Lüssem, Pentacene Schottky diodes studied by impedance spectroscopy: Doping properties and trap response, Phys. Rev. B **88**, 195205 (2013).
[51] I. Katsouras, A. Najafi, K. Asadi, A. J. Kronemeijer, A. J. Oostra, L. J. A. Koster, D. M. de Leeuw, and P. W. M. Blom, Charge transport in poly(p-phenylene vinylene) at low temperature and high electric field, Org. Electron. **14**, 1591 (2013).
[52] P. N. Murgatroyd, Theory of space-charge-limited current enhanced by Frenkel effect, J. Phys. D: Appl. Phys. **3**, 151 (1970).
[53] N. J. van der Kaap, I. Katsouras, K. Asadi, P. W. M. Blom, L. J. A. Koster, and D. M. de Leeuw, Charge transport in disordered semiconducting polymers driven by nuclear tunneling, Phys. Rev. B **93**, 140206 (2016).
[54] F. Wang, X. Qiao, T. Xiong, and D. Ma, The role of molybdenum oxide as anode interfacial modification in the improvement of efficiency and stability in organic light-emitting diodes, Org. Electron. **9**, 985 (2008).
[55] T. Matsushima, G.-H. Jin, and H. Murata, Marked improvement in electroluminescence characteristics of organic light-emitting diodes using an ultrathin hole-injection layer of molybdenum oxide, J. Appl. Phys. **104**, 054501 (2008).
[56] J. Meyer and A. L. Kahn, Electronic structure of molybdenum-oxide films and associated charge injection mechanisms in organic devices, J. Photon. Energy **1**, 011109 (2011).